ACS OMEGA

Open Access

http://pubs.acs.org/journal/acsodf

Article

Low Content Ga_2O_3 Enables the Direct Methane Conversion

Lingling Liang,[#] Shiyun Xiong,[#] and Yong Xu*

Cite This: *ACS Omega* 2024, 9, 25027−25033

Read Online

ACCESS | Metrics & More | Article Recommendations | Supporting Information

ABSTRACT: The direct conversion of methane (CH_4), a main greenhouse gas, to value-added chemicals has attracted increasing attention in order to alleviate the current energy crisis and environmental concern. Nevertheless, the oriented conversion of CH_4 to target product is formidably challenging due to the inertness of CH_4. In this work, we demonstrate that zeolite modified by a low amount of Ga_2O_3 (GS-1) can serve as a highly active and stable catalyst for direct conversion to hydrogen (H_2) and solid carbon. The optimal GS-1 with 0.62 wt % of Ga displays a CH_4 conversion rate of 70.6 mol/g_{Ga}/h with a H_2 productivity of 134 mol/g_{Ga}/h at 800 °C. Analysis on NH_3 temperature-programmed desorption (TPD) and in situ diffuse reflectance infrared Fourier transform spectroscopy (DRIFTS) suggests that the introduction of Ga_2O_3 can poison the acidic site of zeolite and promote the dehydrogenation of CH_4. This work reports a highly active and stable catalyst for direct methane conversion, which may provide a feasible strategy for the sustainable utilization of CH_4.

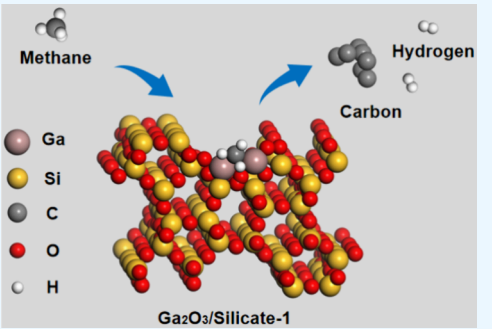

1. INTRODUCTION

As a greenhouse gas, methane (CH_4) is the main component of natural gas and shale gas. Under the current circumstances, the utilization of methane is a clean and sustainable way which has attracted increasing attention to alleviate the current energy crisis and environmental concern.[1,2] To date, CH_4 has been regarded as a cheap and abundant raw material for producing value-added chemicals via C−H activation and C−C coupling. It has been widely reported that CH_4 can be catalytically converted into light olefins, methanol, and aromatic hydrocarbons.[3−5] Nevertheless, the activation of CH_4 generally requires harsh conditions, for example, high temperature, strong oxidizing agent, etc., due to the strong C−H bond in methane.[2,6−8] Moreover, great challenges still remain for converting CH_4 to target product, and the selective activation of CH_4 is of great importance yet challenging.

Given the potential of hydrogen (H_2) in the current energy system, methane, with the highest H/C ratio in alkanes, has been regarded as an ideal raw material for producing hydrogen.[9−11] In principle, CH_4 can be converted into H_2 via indirect catalytic reforming with carbon dioxide (CO_2) or water (H_2O) and direct catalytic decomposition to H_2.[1,12−15] Compared to the indirect process, the direct catalytic decomposition process can produce high purity H_2, which attracts wide interest of researchers. Besides, the direct catalytic decomposition coproduces value-added carbon materials including graphene, carbon nanotubes, and fullerenes, which have been widely used in diverse fields.[15−17] Over the past decades, traditional transition metal catalysts, such as Ni, Mo, Co, Fe, or Pt, can catalyze CH_4 direct decomposition under moderate temperature; however, they suffer from deactivation due to the formation of aromatics, namely coking. Consequently, it is highly desired to develop highly active, thermally stable, and low-cost catalysts for CH_4 direct decomposition.[4,18−23]

In this work, we demonstrate that compositing a low amount of the main group catalyst (i.e., Ga_2O_3) with zeolite (Ga_2O_3/S-1) can significantly promote CH_4 direct conversion to H_2 and carbon. Detailed investigations indicate that the addition of Ga_2O_3 can poison the acidic sites in zeolite, which further suppresses the formation of aromatics (coking) and facilitates the formation of graphited carbon. The optimal Ga_2O_3/S-1 with 0.62 wt % of Ga (i.e., GS-1) displays a CH_4 conversion rate of 70.6 mol/g_{Ga}/h with a H_2 productivity of 134 mol/g_{Ga}/h at 800 °C. Moreover, GS-1 exhibits a superior thermal stability at 800 °C for 60 h, and the H_2 productivity decreases from 134 to 60.7 mol/g_{Ga}/h, which is attributed to the carbon formation on the surface. Impressively, the activity of GS-1 completely returns after removal of the surface carbon. This work provides a main group metal oxide catalyst with low content and superior thermal stability for CH_4 direct conversion, which will attract rapid attention of researchers and promote the fundamental researches on catalyst design.

2. EXPERIMENTAL SECTION

Chemical and Materials. Tetrapropylammonium hydroxide solution (TPAOH, 25 wt %, Macklin Company), tetraethyl

Received: March 4, 2024
Revised: May 16, 2024
Accepted: May 17, 2024
Published: May 30, 2024

orthosilicate (TEOS, 98 wt %, Macklin Company), gallium nitrate hydrate ($Ga(NO_3)_3{\cdot}xH_2O$, Macklin Company), and deionized (DI) water were obtained from Master touch-S15. All of the chemicals were used without any purification.

Synthesis of Silicalite-1 (S-1) Zeolite. The zeolite was prepared via a hydrothermal method.[24] Specifically, 13 g of TPAOH (25 wt %) was mixed with 15 g of DI water under stirring for 10 min, followed by adding 8.32 g of TEOS. After stirring for 6 h, the mixture was transferred into a 100 mL Teflon-lined stainless-steel autoclave and heated at 170 °C for 3 days. Afterward, the Teflon-lined stainless-steel autoclave was naturally cooled to room temperature, and the product was collected by centrifugation by washing with DI water three times. Finally, the resulting catalysts were dried in an oven at 80 °C for 12 h and calcined in air at 550 °C for 6 h.[25]

Synthesis of Zeolite Supported Ga_2O_3 (Ga_2O_3/S-1). Ga_2O_3/S-1 was prepared through a typical wet-impregnation method.[26] The theoretical weight percentage of Ga was set as 1%, 2%, 4%, and 6%, respectively. A certain amount of $Ga(NO_3)_3{\cdot}xH_2O$ was dissolved in 10 mL of deionized water to from a homogeneous solution, which was dropwise added onto the S-1. Typically, for GS-1, 366.8 mg of $Ga(NO_3)_3{\cdot}xH_2O$ was dissolved in 10.0 mL of deionized water, which was dropwise onto 300 mg of S-1 to form a slurry. After aging at 60 °C for 2 h, the slurry was transferred into an oven and dried at 80 °C overnight. Finally, the dried sample was calcinated in a muffle furnace at 600 °C for 2 h. Other catalysts were prepared with a similar strategy except for changing the amount of $Ga(NO_3)_3{\cdot}xH_2O$. The real content of Ga was measured with inductively coupled plasma atomic emission spectroscopy (ICP-AES).

Characterizations. X-ray diffraction (XRD) patterns were collected on a Rigaku Smart Lab 9 kW X-ray diffractometer operating at 40 kV with Cu Kα radiation (λ = 1.541 Å). For the XRD measurement, the step size was 0.02° and the scan speed rate 20°/min. The morphological appearance of the catalyst and deposited carbon was studied with a scanning electron microscopy (SEM) (Hitachi SU8020) operated at 5 kV accelerating voltage. X-ray photoelectron spectroscopy (XPS) was conducted on an Escalab 250 Xi (Thermo-Fisher). High-angle annular dark-field scanning transmission electron microscopy (HAADF-STEM), high-resolution TEM (HRTEM), and energy-dispersive X-ray spectroscopy (EDS) mapping images were recorded on a FEI Talos F200S scanning/transmission electron microscope at 200 kV with a four-quadrant 0.9-sr energy dispersive X-ray spectrometer. Pore size distribution curves and surface areas were measured with a Micromeritics ASAP 2460 system. Inductively coupled plasma optical emission spectrometry (ICP-OES) for determining the composition of catalyst was conducted on Agilent 5110. H_2 temperature-programmed reduction (H_2-TPR) and NH_3 temperature-programmed desorption (NH_3-TPD) measurement was performed on Beishide automatic chemisorption Analyzer C200-0011. Pyridine adsorption infrared spectroscopy (Py-IR) data were collected on a Bruker Tenser 27 FTIR spectrometer. In situ diffuse reflectance infrared Fourier transform spectroscopy (DRIFTS) was conducted on an iS50 Fourier transform infrared spectrometer (Thermo) equipped with a mercury cadmium telluride (MCT) detector. A 20 mg sample was put in the in situ IR cell equipped with a KBr window. The catalyst was pretreated with N_2 at 200 °C for 1 h and then cooled to room temperature. After collecting the background, CH_4 was introduced to the cell to allow the adsorption for 30 min, and then N_2 was flushed to remove the gaseous CH_4 in the cell and the physically adsorbed CH_4 on the surface of the sample for 15 min. Finally, the temperature was increased the target temperature, and the spectra were recorded by collecting 8 scans with a resolution of 4 cm^{-1}.[27] Thermogravimetry analysis was conducted on a TGA4000 (PerkinElmer) in air at the temperature range from 30 to 800 °C with a heating rate of 10 °C/min. Raman spectra were recorded by Raman spectroscopy (inVia Qontor, Renishaw plc) with a laser wavelength of 532 nm.

Catalytic Evaluation. CH_4 direct decomposition was evaluated in a quartz tubular fixed-bed reactor with the inner diameter and length of 1 and 50 cm, respectively. 200 mg of S-1 supported Ga_2O_3 was put in the middle of quartz tubular reactor, and CH_4 was introduced with a mass flow controller. Nitrogen (N_2) was used as the diluent gas. Prior to CH_4 direct conversion, the catalyst was pretreated with 10 vol % H_2/Ar (30 mL/min) at 600 °C for 1 h and then was heated to the target reaction temperature in N_2 with a heating rate of 10 °C/min. For CH_4 decomposition, the flow rates of CH_4 and N_2 were fixed at 4 mL/min with a molar ratio of 1:1. The performance was evaluated by CH_4 conversion, reaction rate, and H_2 productivity with the following equations:

$$\text{CH}_4\ \text{conversion}\ (\%) = \frac{n(\text{CH}_4)_{\text{in}} - n(\text{CH}_4)_{\text{out}}}{n(\text{CH}_4)_{\text{in}}} \times 100\%$$

$$\text{Reaction rate} = \frac{n(\text{CH}_4)_{\text{in}} - n(\text{CH}_4)_{\text{out}}}{m_{\text{Ga}} \times t}$$

$$\text{H}_2\ \text{Productivity} = \frac{n(\text{H}_2)_{\text{out}}}{m_{\text{Ga}} \times t}$$

where n, m, and t represent as the mole of CH_4, the weight of catalyst, and reaction time, respectively. The mole of methane was obtained through the division of the peak area of methane in the GC pattern and that of the standard (methane with a different volume fraction).

3. RESULTS AND DISCUSSION

S-1 was prepared via a classic hydrothermal method (see Experimental Section for detailed information). The SEM image shows that the obtained S-1 displays as a hexagonal prism (Figure 1a). We also prepared a series of catalysts with different amounts of Ga, which were named as GS-2 (1.84 wt %), GS-3 (3.19 wt %), and GS-4 (4.52 wt %), respectively

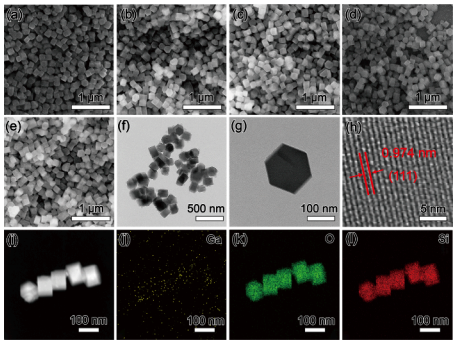

Figure 1. SEM images of (a) GS-1, (b) GS-2, (c) GS-3, (d) GS-4, and (e) S-1. (f,g) TEM and (h) HRTEM images of GS-1. (i–l) HAADF-STEM image and corresponding elemental mappings of GS-1.

https://doi.org/10.1021/acsomega.4c02136
ACS Omega 2024, 9, 25027−25033

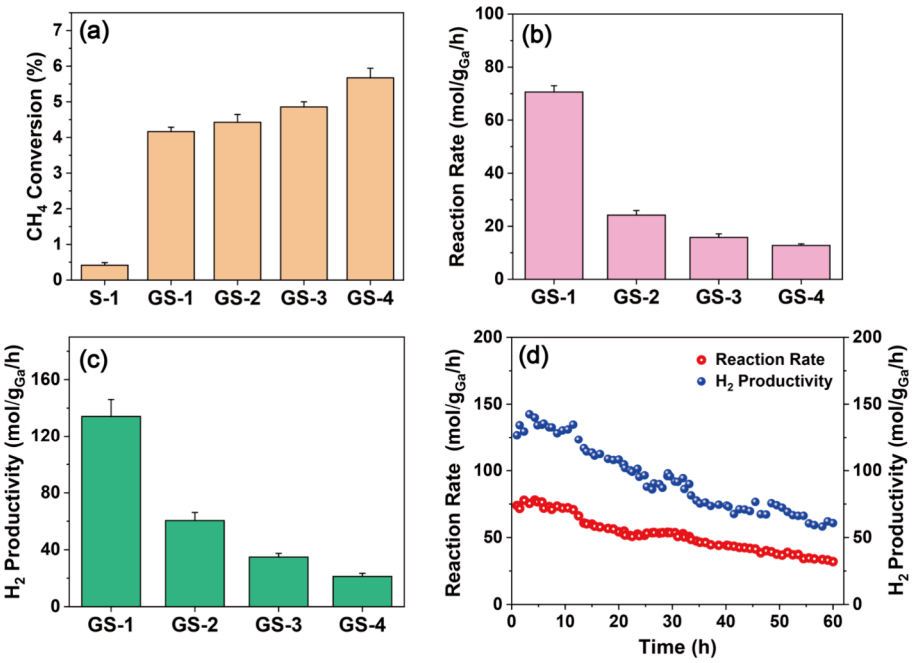

Figure 2. (a) CH_4 conversion, (b) CH_4 conversion rate, and (c) H_2 productivity over GS-1, GS-2, GS-3, and GS-4. (d) Stability test for GS-1. Reaction conditions: CH_4/N_2 = 4:4 mL/min, T = 800 °C, and catalyst weight = 200 mg.

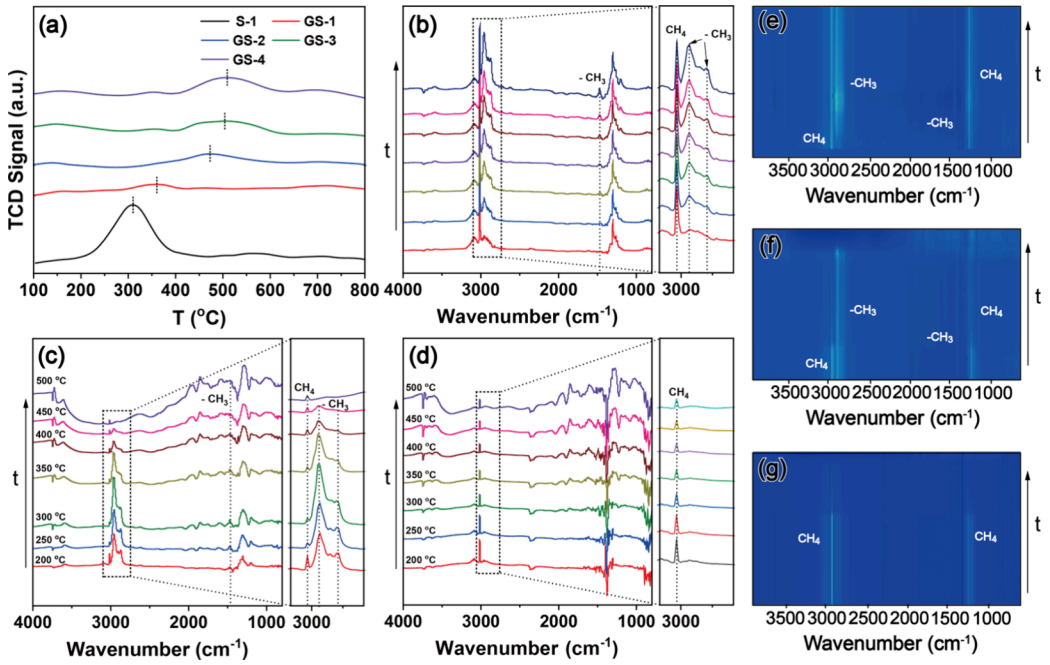

Figure 3. (a) NH_3-TPD spectra of S-1, GS-1, GS-1, GS-2, GS-3, and GS-4. In situ DRIFTS of GS-1 for CH_4 decomposition at (b, e) room temperature and (c, f) other target temperatures. (d, g) In situ DRIFTS of S-1 for CH_4 decomposition at different temperatures.

(Table S1). Note that the loading of Ga_2O_3 negligibly influenced the morphology of S-1, even when the content of Ga was increased to 4.52 wt % (Figure 1b–e). We took GS-1 with 0.62 wt % of Ga as the example for further characterization (Figure 1f). In the TEM image with high magnification, GS-1 presents as a regular hexagonal prism with the edge length of ∼100 nm (Figure 1g), and the lattice distance of 0.974 nm in the HRTEM image is ascribed to the (111) plane of standard silicate oxides (Figure 1h), which further confirms the negligible influence of Ga_2O_3 on the structure of zeolite. Analysis of the HAADF-STEM image and EDS mapping of GS-1 suggests that Ga is evenly distributed on S-1 (Figure 1i–l). Note that the weak intensity of signal of Ga in EDS mapping is attributed to its low loading content. Moreover, XRD patterns were collected to study the structures of various catalysts with different amounts of Ga_2O_3/S-1 (Figure S1). It is found that the peaks in XRD patterns are ascribed to the typical MFI topology structure in the zeolite (PDF: 79-0430).[28] The absence of peaks of Ga_2O_3 in XRD patterns is attributed to its amorphous nature due to low loading amount, further confirming that the structure of S-1 is largely reserved after Ga_2O_3 introduction. Besides, the Ga 2p XPS spectrum of

https://doi.org/10.1021/acsomega.4c02136
ACS Omega 2024, 9, 25027−25033

GS-1 was collected to study the electronic properties of Ga species. The peak at 1117.9 and 1144.9 eV can be indexed as Ga^{3+} $2p_{3/2}$ and $2p_{1/2}$, respectively (Figure S2).[29] Additionally, the N_2 adsorption−desorption measurement was employed to investigate the influence of Ga_2O_3 on the porous structure of MFI (Figure S3). It is found that the surface area slightly decreases from ∼402 to ∼357 m^2/g with increasing Ga content from 0.62% to 4.52%, suggesting that Ga_2O_3 is successfully introduced into the pore of MFI (Table S2).

To reveal the effects of Ga_2O_3 introduction on catalytic performance, S-1 supported Ga_2O_3 with different amounts was used as catalyst for CH_4 decomposition at 800 °C (see detailed information in the Experimental Section). As shown in Figure 2a, the conversion of CH_4 is below 0.5% when only S-1 was used. After introducing Ga_2O_3, the conversion of CH_4 greatly increases to above 4%, suggesting that Ga_2O_3 can strongly promote the decomposition of CH_4. Typically, the CH_4 conversion reaches ∼4.2% when GS-1 (Ga content: 0.62 wt %) was used as the catalyst. Given that the increase of Ga content from 0.62% to 4.52% only leads to the slight increase of CH_4 conversion to ∼5.5%, we thus calculated the conversion rate of CH_4 nominalized by the content of Ga for various catalysts (Figure 2b). Note that the conversion rate of CH_4 decreases from 70.6 to 12.8 mol/g_{Ga}/h when the loading amount of Ga was increased from 0.62% (GS-1) to 4.52% (GS-4), and therefore GS-1 was selected as the optimal catalyst for CH_4 decomposition. Correspondingly, as the only gaseous product, the H_2 productivity reaches 134 mol/g_{Ga}/h over GS-1, which gradually decreases to 21.2 mol/g_{Ga}/h when the loading amount of Ga was increased to 4.52% (GS-4) (Figure 2c). Moreover, CH_4 decomposition is a highly endothermic reaction, and the increase of reaction temperature favors the decomposition of CH_4, as depicted by the increase of CH_4 conversion and H_2 productivity (Figures S4 and S5). In addition, the long-term stability of GS-1 for CH_4 decomposition was evaluated for 60 h. Considering that the formation of carbon will cover the surface of catalyst, the conversion rate of CH_4 and H_2 productivity gradually decreases by 32.0 and 60.7 mol/g_{Ga}/h, respectively, after 60 h (Figure 2d).

More investigations were performed to figure out the mechanism for the enhanced performance toward CH_4 decomposition after Ga_2O_3 introduction. In H_2-TPR curves, no peaks of H_2 consumption were observed in the temperature range 20−800 °C even when the content of Ga was increased to 4.52 wt % (GS-4) (Figure S6), suggesting the strong synergy between Ga_2O_3 and S-1. Considering the acidic sites in catalyst may influence the performance of CH_4 decomposition, NH_3-TPD measurement was carried out to study the acidic properties of various catalysts.[30,31] As shown in Figure 3a, S-1 displays an intense peak around 300 °C in the NH_3-TPD curve. After introducing Ga_2O_3, the peak intensity in the NH_3-TPD curve of GS-1 strongly weakens, and the peak position positively shifts to ∼358 °C, suggesting that the introduction of Ga_2O_3 can greatly reduce the acidic sites (Table S3). However, a further increase of Ga_2O_3 content leads to the increase of NH_3 adsorption, namely, a volcano shape between the acidic sites and the Ga_2O_3 content. Given that the acidic sites favor the formation of coke that may block the active sites, the increase of acidic sites at high content of Ga_2O_3 will lead to a fast coke deposition and decay of the CH_4 conversion rate (Figure 3a and Table S3), being consistent with experimental observations (Figure 2b). Besides, we collected the pyridine-IR (Py-IR) spectrum of GS-1 to investigate the type of acid sites (Figure S7). The absorption peaks at 1445, 1489, 1580, and 1596 cm^{-1} are ascribed to L acid sites, while the absorption peaks at 1489, 1543, and 1639 cm^{-1} can be indexed as B acid sites.[32] Moreover, in situ diffuse reflection Fourier transform infrared spectroscopy (DRIFTS) was employed to evaluate the methane decomposition. First, in situ DRIFTS spectra were collected by introducing CH_4 onto GS-1 at room temperature. As shown in Figure 3b, the intense peaks at 3020 and 1304 cm^{-1} are ascribed to the gaseous CH_4.[33,34] With increasing time, the peaks at ∼2960/2870 and ∼1460 cm^{-1} appear in the in situ DRIFTS spectra, which correspond to the stretching vibration and scissor vibration of $*CH_3$ (Figure 3b).[35] The increasing intensity of the peak of $*CH_3$ indicates the dehydrogenation of CH_4. Furthermore, we increased the temperature to 500 °C during the in situ DRIFTS measurement. It was found that the peak intensities of $*CH_3$ at ∼2960 and 2870 cm^{-1} increase with the temperature to 300 °C (Figure 3c), suggesting that a high temperature favors the dehydrogenation of CH_4. However, further increasing the temperature to 500 °C leads to the decrease of peak intensity of $*CH_3$, which can be attributed to its desorption or further dehydrogenation at high temperature. In sharp contrast, when S-1 without Ga_2O_3 was used as catalyst, the only presence of gaseous CH_4 at 3020 cm^{-1} but the absence of peaks of $*CH_3$ even at 300 °C implies that S-1 is inactivate for CH_4 decomposition (Figure 3d), being consistent with experimental observations. In addition, the peak evolution in DRIFTS spectra during CH_4 decomposition on GS-1 and S-1 has been vividly revealed by the corresponding two-dimensional (2-D) profiles (Figure 3e−g).

To further demonstrate the CH_4 decomposition on GS-1, we took the real pictures of the catalyst bed before and after catalysis. It is noted that the catalyst bed turns from light gray (Figure 4a) to dark black after catalysis (Figure 4b), which is ascribed to the formation of carbon. Moreover, the formation of carbon is further confirmed by the SEM image of the spent GS-1, where the surface of GS-1 is roughened (Figure 4c). Two intense peaks appear in the Raman spectrum of spent GS-1, which correspond to the D and G bands of carbon,

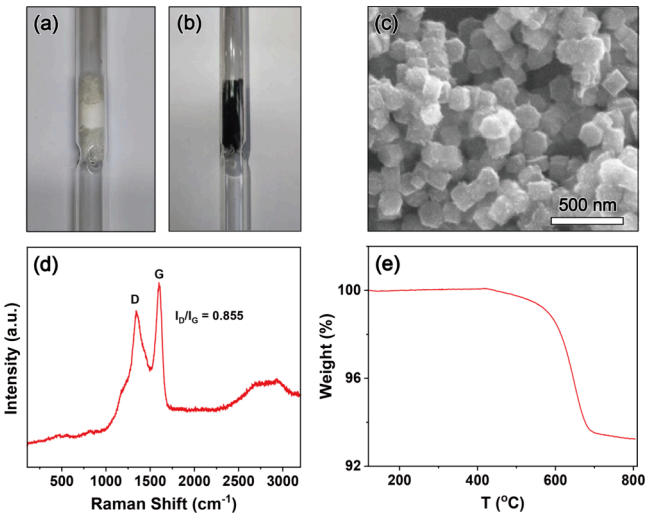

Figure 4. Comparison of catalyst appearance (a) before and (b) after reaction. (c) SEM image of spent catalyst. (d) Raman spectra and (e) TGA characterization of spent catalyst.

https://doi.org/10.1021/acsomega.4c02136
ACS Omega 2024, 9, 25027−25033

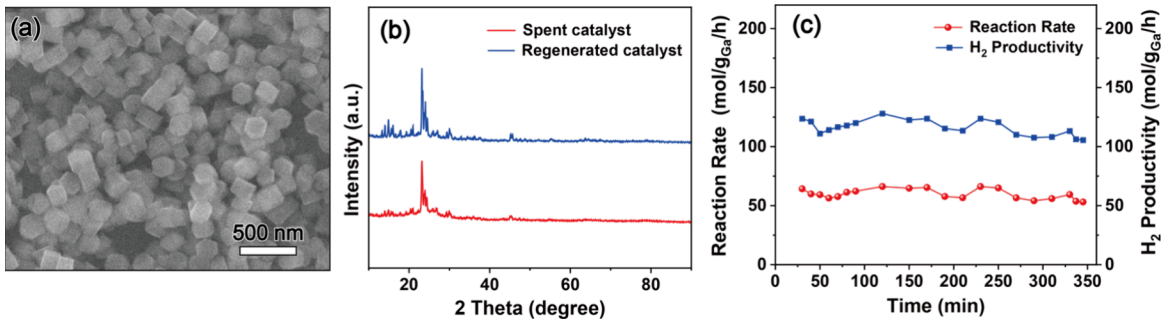

Figure 5. (a) SEM image of the regenerated GS-1. (b) XRD patterns of spent GS-1 and regenerated GS-1. (c) Conversion rates of CH_4 and H_2 productivity and of regenerated GS-1. The regeneration of spent GS-1 was carried out by treating it in air at 750 °C for 0.5 h.

respectively (Figure 4d). The ratio of D/G is ~0.855, suggesting that the formed carbon mainly presents as crystalline graphited carbon.[36] Additionally, the formation of carbon on GS-1 was investigated by thermal gravimetric analysis (TGA) in an air atmosphere in the temperature range from 30−800 °C. As shown in Figure 4e, the weight loss occurs at 400−800 °C, with a sharp loss at ~650 °C, further confirming the formation of graphited carbon.

Given that the formed carbon will deactivate the activity, we treated spent GS-1 after CH_4 decomposition for 60 h in air at 750 °C for 0.5 h. SEM image of the regenerated GS-1 suggests that the formed carbon has been removed from the surface of GS-1 (Figure 5a), while the restoration of the morphology of GS-1 after catalysis and regeneration implies its great thermal stability at high temperature. Compared to the spent GS-1, the presence of the characteristic peaks of S-1 demonstrates the stability, and a slight increase of peak intensity is attributed to carbon removal (Figure 5b). The absence of D/G peaks in the Raman spectrum of the regenerated GS-1 (Figure S8) further confirmed that carbon has been removed during air treatment. Note that the performance in terms of conversion rate and H_2 productivity regain after removing the deposited carbon on the surface of catalyst (Figure 5c), further confirming that the gradual decay of the conversion rate of CH_4 and H_2 productivity in 60 h is attributed to the accumulation of carbon on the surface of catalyst (Figure 2d). The above results demonstrate that GS-1 can serve as a highly active and stable catalyst for CH_4 direct decomposition.

4. CONCLUSION

In summary, we demonstrate that CH_4 can be directly converted into H_2 and carbon over Ga_2O_3-modified zeolite. Detailed investigations show that the introduction of Ga_2O_3 can poison the acidic site of the zeolite and promote the dehydrogenation of CH_4. Impressively, the optimal GS-1 with 0.62 wt % of Ga displays a CH_4 conversion rate of 70.6 mol/g_{Ga}/h with a H_2 productivity of 134 mol/g_{Ga}/h at 800 °C. Moreover, GS-1 displays superior stability toward CH_4 direct decomposition at high temperature, which can be completely regenerated after removing the formed carbon from the surface of catalyst. This work provides a feasible strategy for the conversion of CH_4 into H_2, a promising clean energy carrier, which will attract great interests in chemical industry for the sustainable utilization of CH_4.

■ ASSOCIATED CONTENT

Supporting Information

The Supporting Information is available free of charge at https://pubs.acs.org/doi/10.1021/acsomega.4c02136.

Additional XRD patterns, XPS spectrum, N_2 adsorption−desorption curves, CH_4 conversion of GS-1, H_2 productivity over GS-1, H_2-TPR curves, Py-IR spectrum, Raman spectra, and tables of Ga contents, physical properties, and NH_3-TPD results (PDF)

■ AUTHOR INFORMATION

Corresponding Author

Yong Xu − *Guangzhou Key Laboratory of Low-Dimensional Materials and Energy Storage Devices, Collaborative Innovation Center of Advanced Energy Materials, School of Materials and Energy, Guangdong University of Technology, Guangzhou 510006, China;* Present Address: i-Lab, Suzhou Institute of Nano-Tech and Nano-Bionics (SINANO), Chinese Academy of Sciences (CAS), 398 Ruoshui Road, Suzhou 215123, China; orcid.org/0000-0001-5115-6492; Email: yxu2023@sinano.ac.cn

Authors

Lingling Liang − *Guangzhou Key Laboratory of Low-Dimensional Materials and Energy Storage Devices, Collaborative Innovation Center of Advanced Energy Materials, School of Materials and Energy, Guangdong University of Technology, Guangzhou 510006, China*

Shiyun Xiong − *Guangzhou Key Laboratory of Low-Dimensional Materials and Energy Storage Devices, Collaborative Innovation Center of Advanced Energy Materials, School of Materials and Energy, Guangdong University of Technology, Guangzhou 510006, China*

Complete contact information is available at: https://pubs.acs.org/10.1021/acsomega.4c02136

Author Contributions

#L. Liang and S. Xiong contributed equally to this work. The manuscript was written through contributions of all authors. All authors have given approval to the final version of the manuscript.

Notes

The authors declare no competing financial interest.

■ ACKNOWLEDGMENTS

This work was financially supported by Guangdong Provincial Natural Science Fund for Distinguished Young Scholars

(2021B1515020081), the National Natural Science Foundation of China (12174276), and the start-up support from Guangdong University of Technology.

REFERENCES

(1) Tang, P.; Zhu, Q.; Wu, Z.; Ma, D. Methane activation: The Past and Future. *Energy Environ. Sci.* **2014**, *7*, 2580−2591.
(2) Huang, J.; Liu, W.; Yang, Y.; Liu, B. High-Performance Ni−Fe Redox Catalysts for Selective CH_4 to Syngas Conversion via Chemical Looping. *ACS Catal.* **2018**, *8*, 1748−1756.
(3) Wang, Y.; Li, L.; Li, G.; Zhao, Q.; Wu, X. s.; Wang, Y.; Sun, Y.; Hu, C. Synergy of Oxygen Vacancies and Ni^0 Species to Promote the Stability of a Ni/ZrO_2 Catalyst for Dry Reforming of Methane at Low Temperatures. *ACS Catal.* **2023**, *13*, 6486−6496.
(4) Chen, S.; Li, S.; You, R.; Guo, Z.; Wang, F.; Li, G.; Yuan, W.; Zhu, B.; Gao, Y.; Zhang, Z.; Yang, H.; Wang, Y. Elucidation of Active Sites for CH_4 Catalytic Oxidation over Pd/CeO_2 Via Tailoring Metal−Support Interactions. *ACS Catal.* **2021**, *11*, 5666−5677.
(5) Wang, J.; Jin, L.; Li, Y.; Hu, H. Preparation of Fe-Doped Carbon Catalyst for Methane Decomposition to Hydrogen. *Ind. Eng. Chem. Res.* **2017**, *56*, 11021−11027.
(6) McFarland, E. Unconventional Chemistry for Unconventional Nature Gas. *Science* **2012**, *338*, 340−342.
(7) Zhou, L.; Enakonda, L. R.; Harb, M.; Saih, Y.; Aguilar-Tapia, A.; Ould-Chikh, S.; Hazemann, J.-l.; Li, J.; Wei, N.; Gary, D.; Del-Gallo, P.; Basset, J.-M. Fe Catalysts for Methane Decomposition to Produce Hydrogen and Carbon Nano Materials. *Appl. Catal., B* **2017**, *208*, 44−59.
(8) Rastegarpanah, A.; Rezaei, M.; Meshkani, F.; Zhang, K.; Zhao, X.; Pei, W.; Liu, Y.; Deng, J.; Arandiyan, H.; Dai, H. Influence of Group VIB Metals on Activity of the Ni/MgO Catalysts for Methane Decomposition. *Appl. Catal., B* **2019**, *248*, 515−525.
(9) Jana, P.; de la Pena O'Shea, V. A.; Coronado, J. M.; Serrano, D. P. Co-production of Graphene Sheets and Hydrogen by Decomposition of Methane Using Cobalt Based Catalysts. *Energy Environ. Sci.* **2011**, *4*, 778−783.
(10) Kang, D.; Rahimi, N.; Gordon, M. J.; Metiu, H.; McFarland, E. W. Catalytic Methane Pyrolysis in Molten $MnCl_2$-KCl. *Appl. Catal., B* **2019**, *254*, 659−666.
(11) Wang, H.; Diao, Y.; Gao, Z.; Smith, K. J.; Guo, X.; Ma, D.; Shi, C. H_2 Production from Methane Reforming over Molybdenum Carbide Catalysts: From Surface Properties and Reaction Mechanism to Catalyst Development. *ACS Catal.* **2022**, *12*, 15501−15528.
(12) Yadav, M. D.; Patwardhan, A. W.; Joshi, J. B.; Dasgupta, K. Kinetic Study of Multi-Walled Carbon Nanotube Synthesis by Thermocatalytic Decomposition of Methane Using Floating Catalyst Chemical Vapour Deposition. *Chem. Eng. J.* **2019**, *377*, 119895−119904.
(13) Anish, M.; Bency, P.; Jayaprabakar, J.; Jayaprakash, V.; Rao, P S.; Phanikumar, K.; Kumar, J. A.; Saravanan, A.; Rajasimman, M. Utilization of Nanomaterials in Hydrogen Production-Emerging Technologies and Its Advancements: An Overview. *Int. J. Hydrogen Energy* **2024**, *52*, 140−158.
(14) Fan, Z.; Weng, W.; Zhou, J.; Gu, D.; Xiao, W. Catalytic Decomposition of Methane to Produce Hydrogen: A Review. *J. Energy Chem.* **2021**, *58*, 415−430.
(15) Patlolla, S. R.; Katsu, K.; Sharafian, A.; Wei, K.; Herrera, O. E.; Merida, W. A Review of Methane Pyrolysis Technologies for Hydrogen Production. *Renew. Sust. Energy Rev.* **2023**, *181*, 113323−113335.
(16) Kang, D.; Palmer, C.; Mannini, D.; Rahimi, N.; Gordon, M. J.; Metiu, H.; McFarland, E. W. Catalytic Methane Pyrolysis in Molten Alkali Chloride Salts Containing Iron. *ACS Catal.* **2020**, *10*, 7032−7042.
(17) Palmer, C.; Tarazkar, M.; Kristoffersen, H. H.; Gelinas, J.; Gordon, M. J.; McFarland, E. W.; Metiu, H. Methane Pyrolysis with a Molten Cu−Bi Alloy Catalyst. *ACS Catal.* **2019**, *9*, 8337−8345.
(18) Ji, Y.; Palmer, C.; Foley, E.; Giovine, R.; Yoshida, E.; Sebti, E.; Patterson, A.; McFarland, E.; Clement, R. Valorizing the Carbon Byproduct of Methane Pyrolysis in Batteries. *Carbon* **2023**, *204*, 26−35.
(19) Zeng, J.; Tarazkar, M.; Pennebaker, T.; Gordon, M.; Metiu, H.; McFarland, E. Catalytic Methane Pyrolysis with Liquid and Vapor Phase Tellurium. *ACS Catal.* **2020**, *10*, 8223−8230.
(20) Patzschke, C. F.; Parkinson, B.; Willis, J. J.; Nandi, P.; Love, A. M.; Raman, S.; Hellgardt, K. Co-Mn Catalysts for H_2 Production via Methane Pyrolysis in Molten Salts. *Chem. Eng. J.* **2021**, *414*, 128730−128742.
(21) Chen, L.; Song, Z.; Zhang, S.; Chang, C.-K.; Chuang, Y.-C.; Peng, X.; Dun, C.; Urban, J. J.; Guo, J.; Chen, J.-L.; Prendergast, D.; Salmeron, M.; Somorjai, G. A.; Su, J. Ternary NiMo-Bi Liquid Alloy Catalyst for Efficient Hydrogen Production from Methane Pyrolysis. *Science* **2023**, *381*, 857−861.
(22) Xi, W.; Wang, K.; Shen, Y.; Ge, M.; Deng, Z.; Zhao, Y.; Cao, Q.; Ding, Y.; Hu, G.; Luo, J. Dynamic Co-Catalysis of Au Single Atoms and Nanoporous Au for Methane Pyrolysis. *Nat. Commun.* **2020**, *11*, 1919−1927.
(23) Huang, W.; Bo, T.; Zuo, S.; Wang, Y.; Chen, J.; Ould-Chikh, S.; Li, Y.; Zhou, W.; Zhang, J.; Zhang, H. Surface Decorated Ni Sites for Superior Photocatalytic Hydrogen Production. *Susmat* **2022**, *2*, 466−475.
(24) Dai, C.; Zhang, A.; Li, L.; Hou, K.; Ding, F.; Li, J.; Mu, D.; Song, C.; Liu, M.; Guo, X. Synthesis of Hollow Nanocubes and Macroporous Monoliths of Silicalite-1 by Alkaline Treatment. *Chem. Mater.* **2013**, *25*, 4197−4205.
(25) Sun, Q.; Wang, N.; Fan, Q.; Zeng, L.; Yu, G.; et al. Subnanometer Bimetallic Platinum-Zinc Clusters in Zeolites for Propane Dehydrogenation. *Angew. Chem., Int. Ed.* **2020**, *59*, 19450−19459.
(26) Wu, X.; Zhang, H.; Zuo, S.; Dong, J.; Li, Y.; Zhang, J.; Han, Y. Engineering the Coordination Sphere of Isolated Active Sites to Explore the Intrinsic Activity in Single-Atom Catalysts. *Nano-Micro Lett.* **2021**, *13*, 136−164.
(27) Feng, C.; Bo, T.; Maity, P.; Zuo, S.; Zhou, W.; Huang, K.; Mohammed, O. F.; Zhang, H. Regulating Photocatalytic CO_2 Reduction Kinetics through Modification of Surface Coordination Sphere. *Adv. Funct. Mater.* **2023**, *34* (9), 2309761.
(28) Fang, Y.; Su, X.; Bai, X.; Wu, W.; Wang, G.; Xiao, L.; Yu, A. Aromatization over Nanosized Ga-Containing ZSM-5 Zeolites Prepared by Different Methods: Effect of Acidity of Active Ga Species on the Catalytic Performance. *J. Energy Chem.* **2017**, *26*, 768−775.
(29) Xu, Y.; Wang, X.; Yang, D.; Tang, Z.; Cao, M.; Hu, H.; Liu, J.; Li, Y.; Zhang, Q. Stabilizing Oxygen Vacancies in ZrO_2 by Ga_2O_3 Boosts the Direct Dehydrogenation of Light Alkanes. *ACS Catal.* **2021**, *11*, 10159−10169.
(30) Lee, H.; Park, S.; Song, I.; Jung, J. Direct Synthesis of Dimethyl Carbonate from Methanol and Carbon Dioxide over Ga_2O_3/$Ce_{0.6}Zr_{0.4}O_2$ Catalysts: Effect of Acidity and Basicity of the Catalysts. *Catal. Lett.* **2011**, *141*, 531−537.
(31) Zhang, X.; Huang, W.; Yu, L.; Garcia-Melchor, M.; Wang, D.; Zhi, L.; Zhang, H. Enabling Heterogeneous Catalysis to Achieve Carbon Neutrality: Directional Catalytic Conversion of CO_2 into Carboxylic Acids. *Carbon Energy* **2024**, *6*, No. e362.
(32) Liu, C.; Sun, J.; Brown, H. M.; Marin-Flores, O. G.; Bays, J. T.; Karim, A. M.; Wang, Y. Aqueous Phase Hydrodeoxygenation of Polyols over Pd/WO_3-ZrO_2: Role of Pd-WO_3 Interaction and Hydrodeoxygenation Pathway. *Catal. Today* **2016**, *269*, 103−109.
(33) Campa, M.; Pietrogiacomi, D.; Catracchia, C.; Morpurgo, S.; Olszowka, J.; Mlekodaj, K.; Lemishka, M.; Dedecek, J.; Kornas, A.; Tabor, E. Fe-MOR and Fe-FER as Catalysts for Abatement of N_2O with CH_4: In Situ UV-vis DRS and Operando FTIR Study. *Appl. Catal., B* **2024**, *342*, 123360−123378.
(34) Li, Q.; Gao, Y.; Zhang, M.; Gao, H.; Chen, J.; Jia, H. Efficient Infrared-Light-Driven Photothermal CO_2 Reduction over MOF-

https://doi.org/10.1021/acsomega.4c02136
ACS Omega 2024, 9, 25027−25033

Derived Defective Ni/TiO_2. *Appl. Catal., B* **2022**, *303*, 120905−120916.
(35) Azancot, L.; Bobadilla, L.; Centeno, M.; Odriozola, J. IR Spectroscopic Insights into the Coking-Resistance Effect of Potassium on Nickel-Based Catalyst during Dry Reforming of Methane. *Appl. Catal., B* **2021**, *285*, 119822−119834.
(36) Li, Z.; Deng, L.; Kinloch, I.; Young, R. Raman Spectroscopy of Carbon Materials and Their Composites: Graphene, Nanotubes and Fibres. *Prog. Mater. Sci.* **2023**, *135*, 101089−101147.

https://doi.org/10.1021/acsomega.4c02136
ACS Omega 2024, 9, 25027−25033